Applied Catalysis B: Environmental 188 (2016) 351–359

Contents lists available at ScienceDirect

Applied Catalysis B: Environmental

journal homepage: www.elsevier.com/locate/apcatb

Probing effective photocorrosion inhibition and highly improved photocatalytic hydrogen production on monodisperse PANI@CdS core-shell nanospheres

Chao Wang[a], Li Wang[a,b], Jun Jin[a], Jing Liu[a], Yu Li[a,*], Min Wu[a], Lihua Chen[a], Binjie Wang[d], Xiaoyu Yang[a], Bao-Lian Su[a,b,c,*]

[a] Laboratory of Living Materials at the State Key Laboratory of Advanced Technology for Materials Synthesis and Processing, Wuhan University of Technology, 122 Luoshi Road, 430070 Wuhan, Hubei, China
[b] Laboratory of Inorganic Materials Chemistry (CMI), University of Namur, 61 Rue de Bruxelles, 5000 Namur, Belgium
[c] Department of Chemistry and Clare Hall, University of Cambridge, Lensfeild Road, Cambridge CB2 1EW, United Kingdom
[d] FEI Company, Shanghai Nanoport, 399 Shenxia Road, 201210 Shanghai, China

ARTICLE INFO

Article history:
Received 21 December 2015
Received in revised form 1 February 2016
Accepted 4 February 2016
Available online 6 February 2016

Keywords:
PANI
CdS
Core-shell nanospheres
Photocorrosion inhibition
Photocatalytic hydrogen production

ABSTRACT

CdS is a very good visible-light responsive photocatalyst for hydrogen production. However, the fast recombination of photogenerated electron-hole pairs and quick photocorrosion limit its application in photocatalysis. To address these problems, we herein have designed and synthesized monodisperse polyaniline@cadmium sulfide (PANI@CdS) core-shell nanospheres to probe the mechanisms of photocorrosion inhibition and photocatalytic H_2 production. All the PANI@CdS core-shell nanospheres demonstrate highly enhanced photocorrosion inhibition and photocatalytic hydrogen production comparing to the pure CdS nanospheres. Particularly, the PANI@CdS core-shell nanospheres with the thinnest PANI shell possess the highest hydrogen production rate of 310 μmol h^{-1} g^{-1} in 30 h without deactivation. Our results reveal that the newly formed C—S and/or N—Cd bonds in PANI@CdS prevent the reduction of the surface sulfide ions to sulphur, leading to effective photocorrosion inhibition. Our results also verify that the photogenerated holes migrating from valence band (VB) of CdS to the highest occupied molecular orbital (HOMO) of PANI leads to the enhanced photocatalytic hydrogen production. This work can shed some light on the mechanism of conducting polymers modifying metal sulfides for effective photocorrosion inhibition and highly enhanced photocatalytic activities.

© 2016 Elsevier B.V. All rights reserved.

1. Introduction

Hydrogen, the cleanest and the most environmental friendly energy, has become one of the most research hotspots all around the world [1–4]. Since Fujishima and Honda first reported the photoelectrolysis water on TiO_2 [1], photocatalytic water-splitting for hydrogen production based on semiconductors has aroused much attention in recent years [5–7]. Among the semiconductors for photocatalysis, CdS with a band gap of 2.4 eV is considered to be a high visible-light responsive material for photocatalytic hydrogen production [3,8]. At present, many kinds of materials, such as transition metal oxides [9,10], carbon nanomaterials [11,12] and conducting polymers [13], have been adopted to modify the CdS nanostructures for enhanced photocatalytic activities. However, the study on photocorrosion inhibition is still limited. In fact, photocorrosion largely restricts its further application as highly efficient photocatalyst for hydrogen production [14,15].

Generally, photocorrosion, where surface sulfide ions are oxidized to sulphur by photogenerated holes [14], makes CdS highly unstable as a photocatalyst. According to our density of state (DOS) calculation, the bottom of conduction band (CB) is mainly derived from Cd *3d* orbitals, whereas the top of valence band (VB) of CdS is primarily derived from S *2p* orbitals as illustrated in Scheme 1a. In addition, as an n-type semiconductor, the intrinsic surface defect states can greatly affect its behaviour. When irradiated by solar light, the photogenerated electrons in the outer surface (OS) move to the inner surface (IS) and the photogenerated holes move in the reverse direction. This results in a *p*-type layer at the surface (Scheme 1b). Namely, the interior photogenerated holes continuously escalate the photocorrosion of the outer surface. This leads to fast deactivation of CdS via concentrating in bonding orbital regions of surface sulphur. As photocatalysis occurs at the surface of the photocatalysts, modifying the surface of CdS nanostructures

* Corresponding authors.
E-mail addresses: yu.li@whut.edu.cn, manliyu2002@gmail.com (Y. Li), baoliansu@whut.edu.cn, bls26@cam.ac.uk, bao-lian.su@unamur.be (B.-L. Su).

http://dx.doi.org/10.1016/j.apcatb.2016.02.017
0926-3373/© 2016 Elsevier B.V. All rights reserved.

to stabilize surface sulfide ions and to export surface photogenerated holes is thus crucial for photocorrosion inhibition. Further, the surface modification would also be beneficial for photocatalytic hydrogen production because of the effective separation of photogenerated electron-hole pairs.

Among the materials modifying the surface of CdS nanostructures, conducting polymers have aroused a great interest due to their high conductivity and stability, simple synthesis and good environmental compatibility [16,17]. In particular, polyaniline (PANI) has been considered as a promising material to overcome the intrinsic drawbacks of CdS via efficiently facilitating carriers transfer, owing to the well-matched energy level [18–20]. Although PANI/CdS composites have demonstrated obvious improved photocatalytic activity and photocorrosion inhibition, the mechanism of photocatalysis and photocorrosion inhibition has not been deeply discussed [19–22]. Therefore, through probing the mechanisms of photocatalytic improvement and photocorrosion inhibition of PANI modified CdS composites, it is possible to find the resolution for its further photocatalytic applications.

Herein, we have used a proton doped in-situ polymerization technique to coat a homogeneous and tailorable PANI thin layer on the porous CdS nanospheres to construct PANI@CdS core-shell nanospheres as illustrated in Scheme 1c. Our results show that uniform PANI shell has been successfully coated on CdS surface. Due to the newly formed C—S and/or N—Cd bonds between PANI shell and CdS core, photocorrosion has effectively been inhibited. Particularly, the photocatalytic hydrogen production rates of PANI@CdS core-shell photocatalysts are largely improved, owing to photogenerated holes migrating from VB of CdS to HOMO of PANI. The thinnest PANI shell on CdS nanospheres exhibits the highest photocatalytic hydrogen production rate of 310 μmol h^{-1} g^{-1} in 30 h without deactivation.

2. Experimental

2.1. Materials

All reagents are analytical purity and used without further purification. Cadmium nitrate tetrahydrate, ammonium persulfate, thiourea and ethylene glycol are purchased from Shanghai Aladdin Industrial Corporation. Polyvinylpyrrolidone (PVP, M_W = 58000) is purchased from Sigma-Aldrich Chemistry Corporation. Oxalic acid ($H_2C_2O_4$), aniline and ethanol are purchased from Sinopharm Chemical Reagent Beijing Corporation.

2.2. Calculations of the electronic structures of CdS

Geometrical structure of the optimized 3 × 3 × 1 supercells of CdS nanocrystal as theoretical modelling is constructed without disorders. The partial DOS plots of CdS are obtained by using the first-principles density functional theory (DFT) calculations. The plane-wave-pseudo potential approach is performed using Perdew–Burke–Ernzerhof generalized gradient approximation. A kinetic energy cutoff of 380 eV and k-point sampling with 0.05 $Å^{-1}$ separation in the Brillouin zone are applied. The calculated partial density of states of CdS nanocrystal is illustrated in Scheme 1a.

2.3. Porous CdS nanospheres synthesis

The monodisperse porous CdS nanospheres are prepared via solvothermal method according to a previous process with slight modification [23]. Briefly, 1.54 g $Cd(NO_3)_2{\cdot}4H_2O$ is dissolved into 80 mL ethylene glycol. 1 g PVP is then injected into the above solution and stirred vigorously until homogeneous. 0.38 g thiourea is dissolved in above homogeneous solution and transferred into a 100 mL Teflon-lined stainless steel autoclave. The autoclave is sealed and heated at 160 °C for 8 h and then is cooled to room temperature. The obtained bright-yellow precipitates are purified with distilled water and ethanol for several times. Finally, after dried in oven at 60 °C for 4 h, porous CdS nanospheres are obtained.

2.4. PANI@CdS core-shell nanospheres synthesis

The PANI@CdS core-shell nanospheres are synthesized as following: 0.2 g porous CdS nanospheres are dispersed in 20 mL 0.5 mM oxalic acid ($H_2C_2O_4$) aqueous solution. 0.13 g aniline is added into the above solution and the mixture is rapidly stirred for 1 h. At last, 10 mL 0.5 mM $H_2C_2O_4$ aqueous solution including ammonium persulfate initiator is added in the above mixture and is further stirred for 6 h at room temperature. The obtained PANI@CdS core-shell nanospheres are filtered and washed several times with distilled water. In addition, the thickness of PANI shell

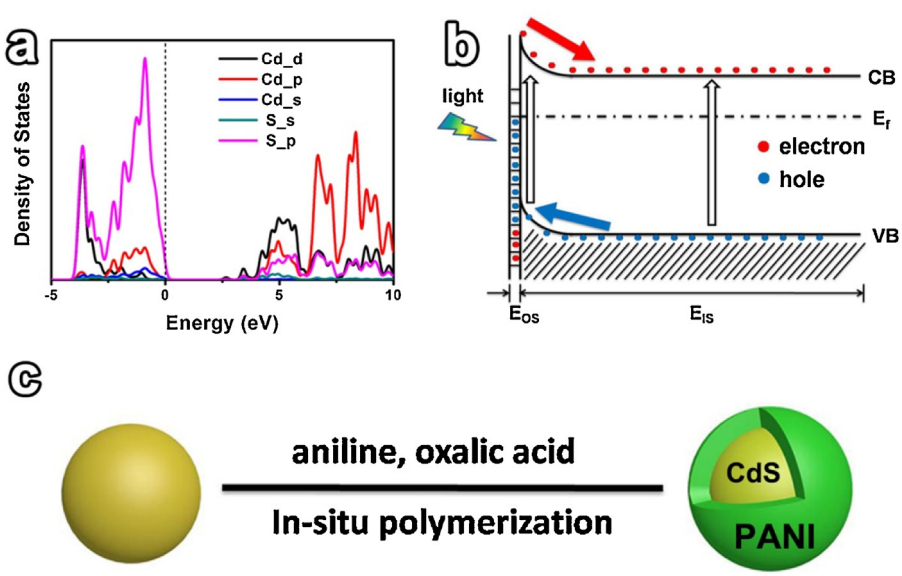

Scheme 1. (a) partial DOS for the electronic orbital of Cd and S atoms, (b) migration of the photogenerated electron-hole pairs in the outer surface (OS) and in the inner surface (IS) under solar light irradiation and (c) schematic illustration of PANI shell coating on the CdS nanospheres surface.

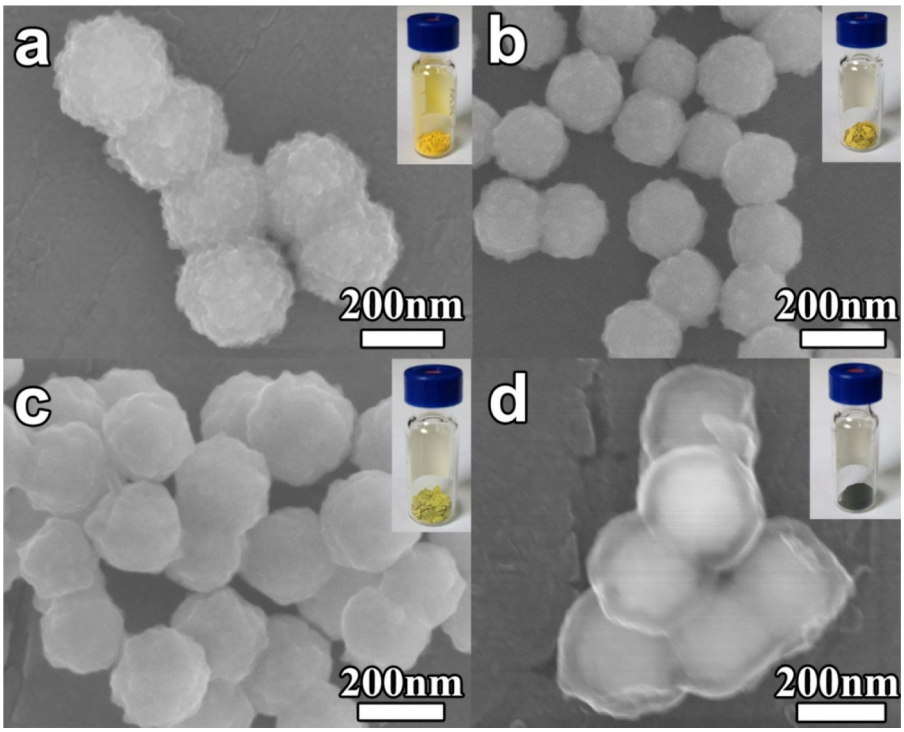

Fig. 1. SEM images of the porous CdS nanospheres and PANI@CdS core-shell nanospheres: (a) CdS nanospheres, (b) PANI@CdS-1, (c) PANI@CdS-1.5 and (d) PANI@CdS-2. The insets are the optical photographs of the corresponding samples. (For interpretation of the references to colour in the text, the reader is referred to the web version of this article.)

can be controlled by adjusting amount of aniline from 0.13 g to 0.26 g. The molar ratio of aniline, oxalic acid and ammonium persulfate is 1:1:1.5. Thus the products are defined as PANI@CdS-N (N = 1, 1.5, 2), where N is the molar ratio of PANI to CdS.

2.5. Characterizations

Powder X-ray diffraction patterns are obtained on an X-ray diffractometer (D8 Advance, XRD) using Cu Kα irradiation source (λ = 1.54056 Å) at a scan rate of $0.05^{\circ}\,s^{-1}$. The morphology and microstructure of prepared samples are characterized by field emission scanning electron microscope (FESEM) S-4800 (HITACHI, Japan). Transmission electron microscopy (TEM), high resolution transmission electron microscopy (HRTEM), high angle annular dark field-scanning transmission electron microscopy (HAADF-STEM) and scanning transmission electron microscopy-electron dispersive X-ray spectroscopy (STEM-EDS) are acquired on a FEI Talos F200X. UV–vis diffused reflectance spectra and UV–vis transmittance spectra of the samples are obtained on a UV–vis spectrophotometer (UV2550, Shimadzu, Japan). Emission spectra of the samples are obtained on a photofluorescence (PL) spectrophotometer (LS55, PerkinElmer, USA) with $BaSO_4$ as a reflectance standard. Fourier-transform infrared (FT-IR) spectra are obtained using an FT-IR spectrophotometer (Thermo Nicolet 360). X-ray photoelectron spectroscopy (XPS) is worked out with a customized X-ray photoelectron spectrometer (VG Multilab 2000-X equipped with a monochromatic Al Kα source). UPS is employed on an AXIS Ultra-DLD-600W ultrahigh vacuum system (a base pressure of 3×10^{-10} m Torr) with HeI excitation (21.22 eV) and monochromatic Al Kα source.

2.6. Photocatalytic activity evaluation

Photocatalytic hydrogen production is performed in a top-irradiation Pyrex cylindrical vessel. The effective irradiation area for the vessel is 28 cm^2 and the visible-light source is 10 cm away from the Pyrex vessel. Typically, 100 mg photocatalysts are dispersed in 100 mL aqueous solution containing 0.1 M Na_2SO_3 and 0.1 M Na_2S as sacrificial reagents by a magnetic stirrer in the Pyrex cylindrical vessel. Then the vessel is connected to a gas circulation system (LabSolar H_2-production system). The photocatalystis irradiated under visible light ($\lambda \geq 420$ nm) with a 300 W Xe lamp. The incident light intensity at the location of catalyst is 100 mW cm^{-2}. The reaction temperature is maintained at 20 °C by cooling water during the whole photocatalytic process. The produced hydrogen is analyzed by an on-line thermal conductivity detector (TCD) gas chromatograph (NaX zeolite column, nitrogen as a carrier gas, Agilent 7890A).

3. Results and discussion

FESEM is employed to investigate the morphology of the CdS nanospheres and PANI@CdS core-shell nanospheres. Fig. 1a shows that the CdS nanospheres have a rough surface with uniform size of 180 nm. Fig. 1b–d present SEM images of the PANI@CdS composites, which clearly demonstrate that the surface of CdS nanospheres gradually becomes smooth with PANI shell thickness increase. The inserted photographs show that the colours of the composites are gradually changed from the yellow of CdS to light green (PANI@CdS-1), green (PANI@CdS-1.5) and dark green (PANI@CdS-2). In particular, the PANI shell and CdS core can clearly been seen for PANI@CdS-2 (Fig. 1d). The photographs and SEM observations indicate that the PANI shell is uniformly coated on the surface of porous CdS nanospheres. Ultrasonic treatment is used to evaluate the toughness of PANI shell on PANI@CdS composites. After 30 min sonication, the PANI shell cannot be peeled off from the CdS nanospheres, indicating strong interaction between CdS and PANI.

The XRD measurement is carried out to determine the crystalline structure of PANI, CdS and PANI@CdS composites (Fig. 2). All the peaks of porous CdS nanospheres are well identified as

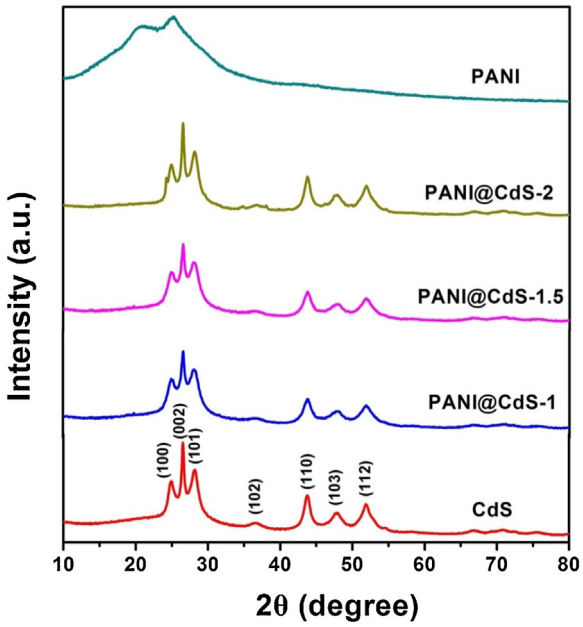

Fig. 2. The XRD patterns of proton-doped PANI, porous CdS nanospheres and PANI@CdS core-shell nanospheres.

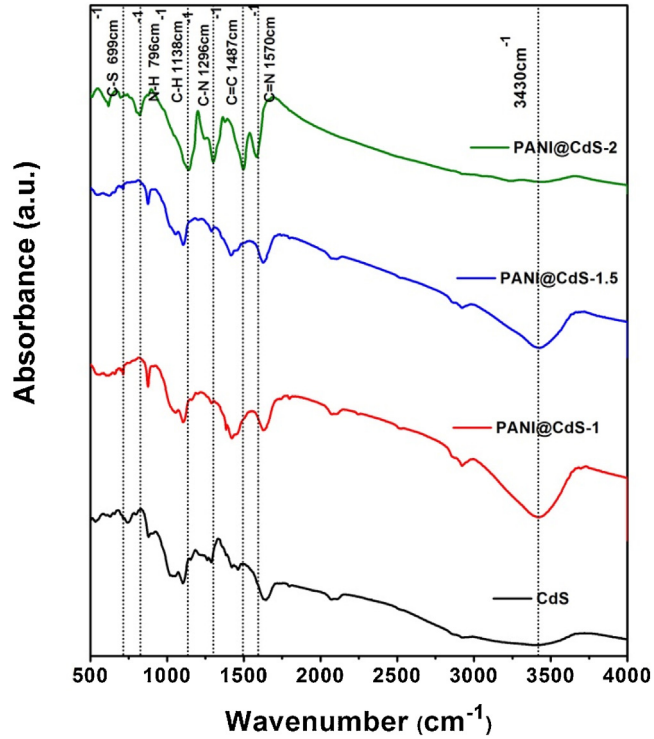

Fig. 3. FTIR spectra of proton-doped PANI, porous CdS nanospheres and PANI@CdS core-shell nanospheres.

hexagonal wurtzite CdS (JCPDS No.41-1049). The XRD patterns of PANI@CdS core-shell nanospheres have no change in peaks and shapes, comparing to porous CdS nanospheres. The three strong peaks for all the samples at 24.8°, 26.5° and 28.3° can be indexed to (1 0 0), (0 0 2) and (1 0 1) crystal planes of hexagonal wurtzite CdS, respectively. The two broad peaks centering at 18° and 25° for PANI are attributed to the periodicity perpendicular and parallel to the polymer chain, respectively [20]. The XRD results indicate that coating PANI shell has no influence on CdS crystal structure.

FT-IR is used to verify the interaction between CdS and PANI (Fig. 3). The peaks at 1570 cm^{-1} and 1487 cm^{-1} are identified to C=N and C=C stretching deformation of quinoid and benzenoid rings, respectively. The peak at 1138 cm^{-1} is C—H in-plane bending vibration. The peaks at 1296 cm^{-1} and 796 cm^{-1} correspond to C—N stretching vibration mode and N—H out-of-plane deformation vibration mode, respectively [20]. And the typical peaks of PANI@CdS-1 and PANI@CdS-1.5 are similar to those of CdS, except for a little shift or intensity decrease. Indeed, the chemical bonds are influenced due to the interaction between PANI and the surface dangling bonds of CdS nanospheres. C—H in-plane bending vibration at 1138 cm^{-1}, C=C stretching vibration at 1487 cm^{-1} and C—N stretching vibration at 1296 cm^{-1} become weaker. The weak peak at 3430 cm^{-1} is attributed to N—H stretching vibration mode. And the relatively weak peak at 699 cm^{-1} is associated to the C—S bond in PANI@CdS [24]. It provides the evidence of the strong interaction between PANI and CdS. It is noted that the spectrum of PANI@CdS-2 is quite similar to PANI, indicating that the thickness of PANI shell can affect the photons transmittance and influence the light absorption and utilization. This is further verified by the UV–vis transmittance measurement of the PANI films obtained at the same synthesis conditions for PANI@CdS (Fig. S1). It clearly shows that the PANI-1 film demonstrates better photons transmittance than the PANI-2 film. This is very important for photocatalytic hydrogen production.

TEM and HRTEM are conducted to reveal the detail structure of porous CdS nanospheres. TEM image shows that the porous CdS nanospheres are constructed by small nanoparticles (Fig. S2a). The lattice fringes of 0.299 nm and 0.22 nm from HRTEM image correspond to the (1 0 1) and (1–10) crystal plane of hexagonal wurtzite CdS respectively (Fig. S2b), in good agreement with XRD result.

Fig. 4 depicts the typical TEM, HAADF-STEM and corresponding STEM-EDS elemental mapping images of PANI@CdS core-shell nanospheres. The surface of PANI@CdS-1 is still rough, similar to the porous CdS nanospheres (Fig. 4a). The HRTEM image clearly displays the lattice fringes of CdS (Fig. S3), indicating ultrathin layer of PANI at the surface. Upon our intensive observations, no PANI is obviously found in PANI@CdS-1. On the contrary, PANI@CdS-1.5 and PANI@CdS-2 display distinct PANI shell at the surface of porous CdS nanospheres (Fig. 4c–e). The thickness of PANI shell is at ~16 nm for PANI@CdS-1.5 (Fig. S4) and at ~20 nm for PANI@CdS-2 (Fig. S5). HAADF-STEM images and STEM-EDS elemental mappings give more information of PANI shell on CdS nanospheres. Although PANI shell has not been observed on PANI@CdS-1, the elemental mappings obviously demonstrate that C and N elements uniformly distribute on porous CdS nanospheres (Fig. 4b), suggesting the homogeneous ultrathin PANI shell. Both PANI@CdS-1.5 and PANI@CdS-2 clearly show the core-shell structure (Fig. 4d–f).

As the PANI shell is not obviously displayed by two-dimensional STEM-EDS elemental mapping on PANI@CdS-1, three-dimensional STEM-EDS tomography is then further used to provide explicit confirmation of PANI@CdS-1 core-shell nanospheres (Fig. 5). It is worth to note that the signal of N element in PANI is too weak. Thus, C element is used to show the PANI shell. Fig. 5a-c demonstrates the uniform distributed Cd, S and C elements, respectively. Fig. 5d superimposes Cd, S and C elements together, clearly verifying ultrathin PANI layer uniformly coated on porous CdS nanosphere.

UV–vis absorption is further used to investigate the interaction between CdS core and PANI shell. Fig. 6a shows the spectra of CdS, PANI@CdS-1 and PANI@CdS-1.5, revealing light absorption in the visible-light region. The absorption edge around 525 nm confirms that the band gap is due to the intrinsic transition of CdS nanospheres, hinting that the band gap for CdS nanospheres is of the direct type and the fundamental absorption edge obeys

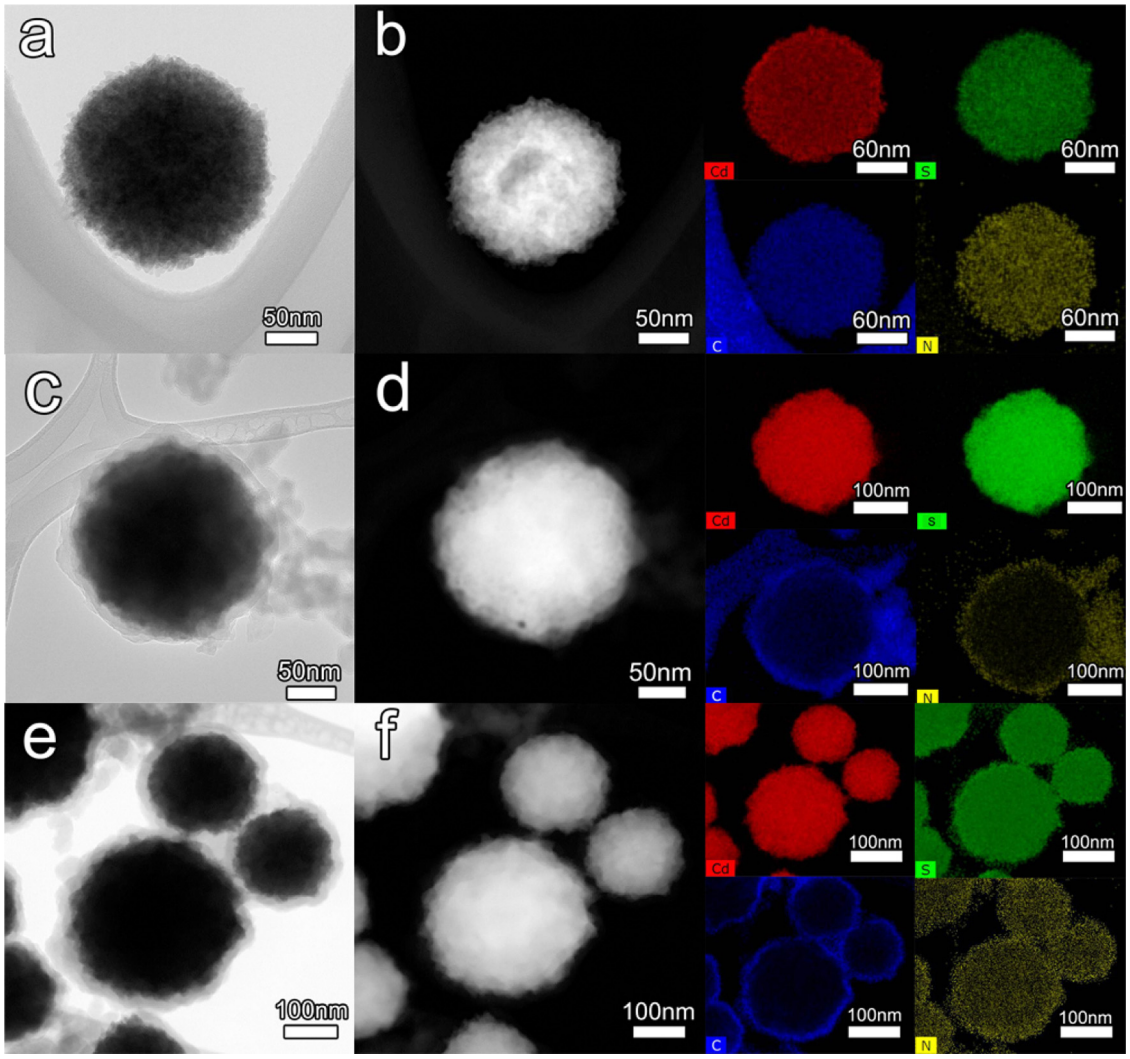

Fig. 4. TEM, HAADF-STEM and STEM-EDS elemental mapping images of the PANI@CdS core-shell nanospheres: (a and b) PANI@CdS-1, (c and d) PANI@CdS-1.5 and (e and f) PANI@CdS-2.

Urbach's rule. Thus the equation $(\alpha E_{photon})^2 = K\ (E_{photon} - E_g)$ is applied to evaluate the band gap energies, where α is the absorption coefficient, E_{photon} is the discrete photon energy, K is a constant, and E_g is the band-gap energy [25,26]. The plot of $(\alpha E_{photon})^2$ vs. photon energy based on the direct transition is shown in Fig. 6a inset. The extrapolated value (the straight lines to the x axis) of E_{photon} of CdS, PANI@CdS-1 and PANI@CdS-1.5 gives the absorption edge energy of 2.49 eV, 2.46 eV and 2.48 eV respectively, which means that the PANI@CdS composites can still utilize visible-light photons for photocatalytic hydrogen production.

PL emission spectra are useful to reveal the efficiency of photogenerated carrier trapping, migration, transfer, separation and recombination. Fig. 6b presents the PL emission spectra of CdS and PANI@CdS composites. Comparing to porous CdS nanospheres, the intensity of the PANI@CdS composites displays a considerable fluorescence decrease. The quenched fluorescence indicates effective separation of photogenerated eletron-hole pairs, indicating enhanced photocatalytic H_2 production for PANI@CdS composites. It is interesting to note that the PL emission peak slightly blue-shifts from ~522 nm for CdS to ~510 nm for PANI@CdS composites. Most possibly, this slight blue-shift comes from the strong interaction between PANI and CdS.

X-ray photoelectron spectroscopy (XPS) is carried out on proton-doped PANI, porous CdS nanospheres and PANI@CdS-1 core-shell nanospheres to reveal more detail interaction between PANI and CdS. Fig. S6 presents the survey spectra of PANI and PANI@CdS-1. The typical three peaks of C *1s* binding energies of PANI are at 284.4, 285.6 and 287.5 eV (Fig. 7a), corresponding to C—H or C—C, C—N and C=N respectively [22]. The N *1s* spectrum of PANI gives quininoid diimine at 398.9 eV, benzenoid imine at 399.7 eV and protonation imine at 400.8 eV (Fig. 7b). The binding energies of C—C or C—H, C—N and C=N of PANI@CdS-1 downshift a little to 284.2, 285.3 and 287 eV respectively, owing to new C—S bond formation (Figs. 3 and 7c). This phenomenon is similar to hole-injecting semiconductors for organic light-emitting diodes, where the HOMO's binding energies of organic semiconductors are decreased [27]. It indicates that the photogenerated holes can migrate from VB of CdS to HOMO of PANI under light irradiation, resulting in photocatalytic efficiency improvement. After PANI modification, the N *1s* peak at 399.7 eV decreases to 399.6 eV (Fig. 7d). In particular, the intensity is increased. According to the previous work [28,29], this binding energy decrease means the formation of new metal-N bond. Namely, the peak at 399.6 eV is related to N—Cd formation. It is noted that compared to porous CdS nanospheres, both the binding energies of Cd and S significantly increase for PANI@CdS-1 (Fig. 7e and f), suggesting that Cd and S on the surface simultaneously act as a kind of electron donor state [30], consistent with C *1s* and N *1s* results. More importantly, the

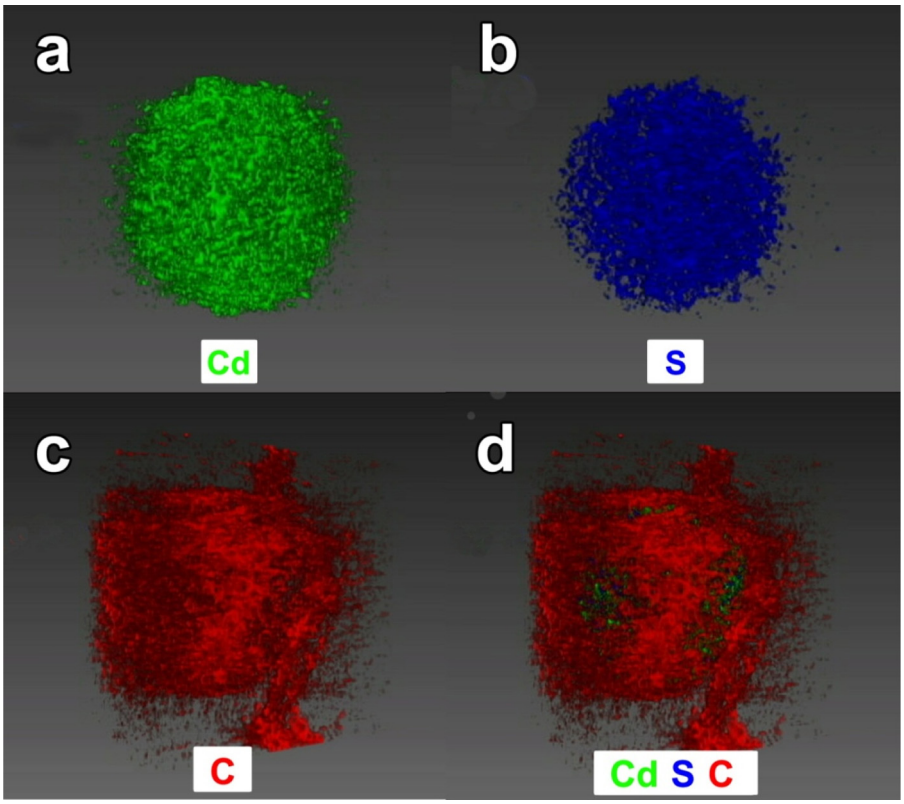

Fig. 5. Three-dimensional STEM-EDS tomography of PANI@CdS-1: (a) green for cadmium, (b) blue for sulfide, (c) red for carbon and (d) montage image. (For interpretation of the references to colour in this figure legend, the reader is referred to the web version of this article.)

peak of S *2p3/2* shifts from 151.9 eV in CdS to 152.7 eV in PANI@CdS-1. The increased binding energy of surface atoms suggests that the PANI@CdS-1 be more stable under visible-light irradiation comparing to the CdS nanospheres.

Photocatalytic performance of the CdS nanospheres and PANI@CdS core-shell nanospheres for hydrogen production is then evaluated under visible-light irradiation in Na_2SO_3 and Na_2S aqueous solution. Fig. 9a demonstrates that the CdS nanospheres produce hydrogen at an evolution of 642.7 μmol g^{-1} at the first 5 h. Then, the photocatalytic activity of the porous CdS nanospheres significantly decreases to 106.3 μmol g^{-1} after 30 h visible-light irradiation. The significant decrease in hydrogen production of CdS is attributed to the quick photocorrosion (the black S can be obviously observed) and fast recombination of photogenerated electrons and holes [31–33]. The hydrogen evolution amounts of all PANI@CdS core-shell nanospheres are improved, indicating that the PANI shell at the surface not only enhances the separation of photogenerated electrons and holes, but also inhibits photocorrosion of CdS. The PANI@CdS-1 exhibits the best photocatalytic hydrogen production, which is over 2 times than porous CdS nanospheres at the first 5 h. A total hydrogen amount of 9429.7 μmol g^{-1} is achieved after 30 h. However, the PANI@CdS-2 has the worst photocatalytic hydrogen production among the PANI@CdS composites. Most possibly, the thicker PANI shell on the surface of PANI@CdS-2 prevents light penetration and absorption (Fig. S1), leading to less photogenerated electrons and holes. These results indicate that the PANI shell can enhance the photocatalytic hydrogen production and proper thickness of PANI shell is very important for photocatalytic activity enhancement.

Fig. 8a also displays the stable hydrogen production on PANI@CdS core-shell nanospheres for 6 cycles, indicating that the PANI shell can keep the porous CdS nanospheres from

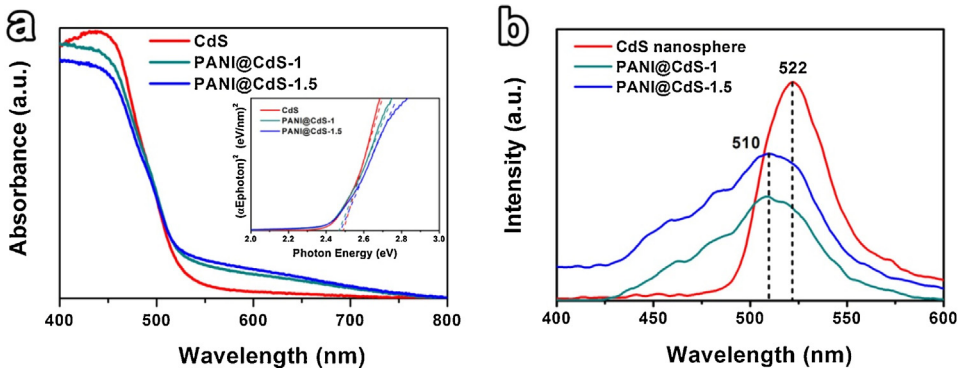

Fig. 6. (a) UV–vis diffusion reflectance spectra and (b) PL spectra of CdS, PANI@CdS-1 and PANI@CdS-1.5. The inset in (a) is the corresponding $(\alpha Ephoton)^2$ vs. photon energy curves. The excitation wavelength is 365 nm for PL emission.

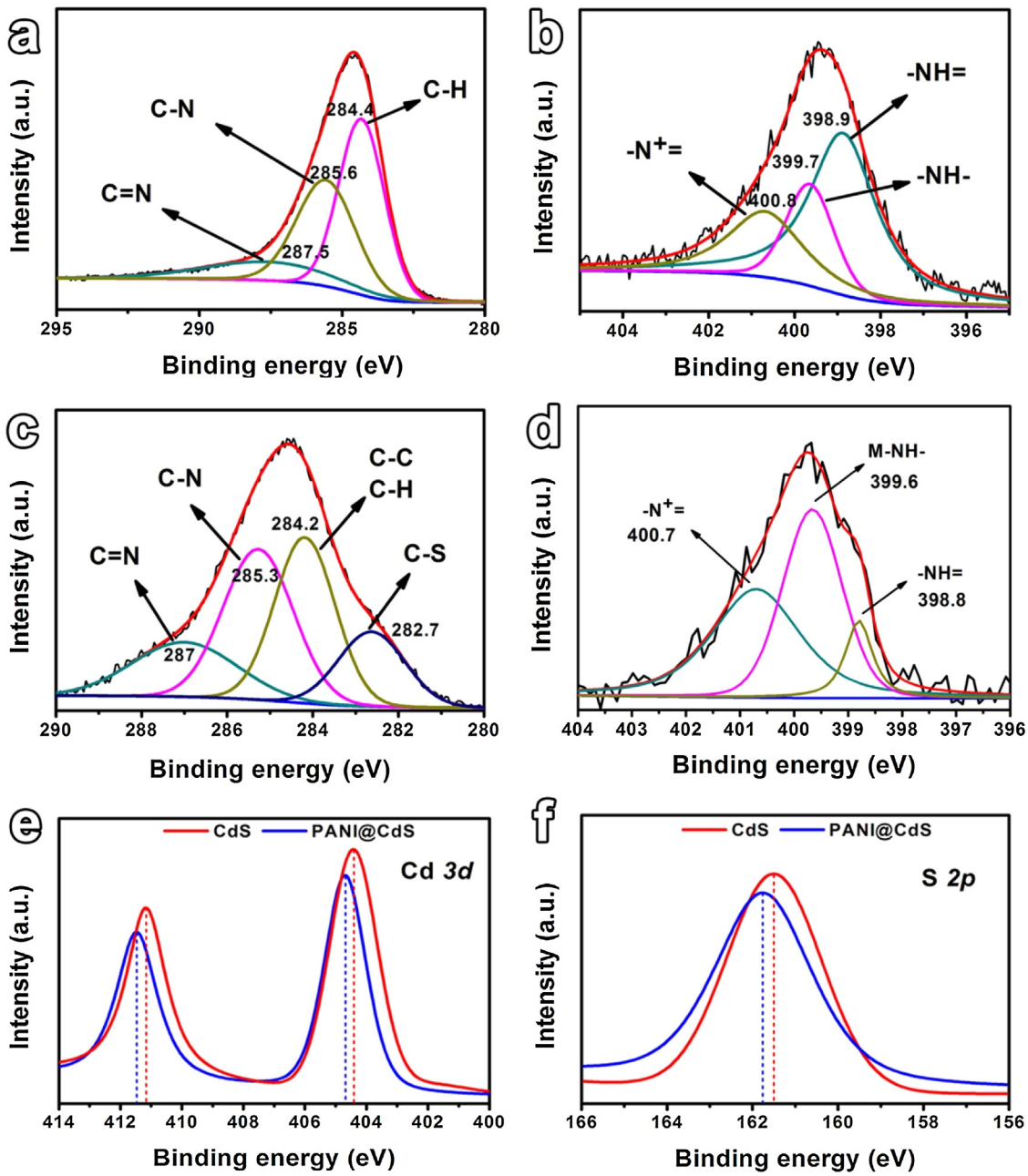

Fig. 7. The XPS spectra of PANI, CdS and PANI@CdS-1: (a) C *1s* and (b) N *1s* spectrum of PANI; (c) C *1s* and (d) N *1s* spectrum of PANI@CdS-1; (e) Cd *3d* and (f) S *2p* spectrum of CdS and PANI@CdS-1, respectively.

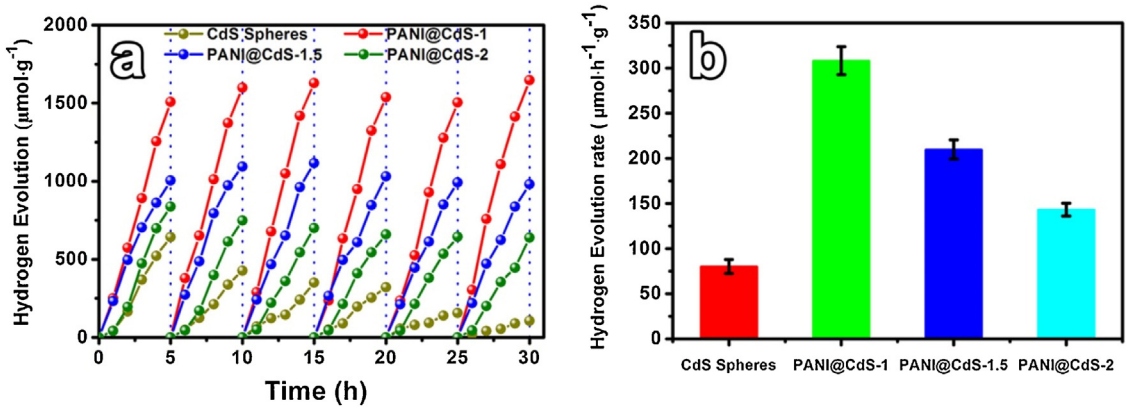

Fig. 8. The photocatalytic hydrogen production rates of porous CdS nanospheres and PANI@CdS core-shell nanospheres. (a) Rate curves and (b) Volume histogram.

photocorrosion. From the FTIR and XPS results, we attribute the effective photocorrosion inhibition to the newly formed C—S and/or N—Cd bonds, preventing the tangling sulphur atoms exposed in the surface of the PANI@CdS core-shell nanospheres. Fig. 8b presents the hydrogen evolution rates for all the samples. The average hydrogen amount produced on CdS is 80.3 μmol h^{-1} g^{-1}. The average hydrogen amounts from PANI@CdS-1, PANI@CdS-1.5 and PANI@CdS-2 are 309.5, 211.5 and 143.7 μmol h^{-1} g^{-1}, which are almost 4, 3 and 2 times to that of CdS nanospheres, respectively. This result is higher than some other nanomaterials modifying CdS nanostructures [34,35], indicating that conducting polymers modifying CdS is an efficient way for photocatalytic activity and photocorrosion enhancement. XPS characterization is further performned on the reacted CdS nanospheres and PANI@CdS-1 after 6 cycles (Fig. S7). The peak at 163.8 eV is related to elemental S [36]. It clearly shows that the PANI@CdS-1 produces a very small amount of elemental S comparing to pure CdS nanospheres after 30 h visible-light irradiation. Therefore, it verifies that the PANI shell can effectively inhibit CdS photocorrosion.

To reveal the mechanism of the photocatalytic hydrogen production, the surface properties of CdS and PANI@CdS-1 are further investigated by UPS measurement to determine their electronic structures. Fig. 9a and b presents the UPS spectra in valence band region and secondary electron cutoff region, respectively. Linear extrapolation is used to determine the positions of valence band maximum (E_{VBM}) and secondary electron cutoff (E_{SECO}) positions. By measuring the width of the emitted electrons from the onset of the secondary electrons up to the Fermi edge and subtracting E_{SECO} from the energy of the incident UV light ($h\gamma$), the work function (φ) can be given by the following formula [37]:

$$\varphi = h\gamma - E_{SECO}. \quad (1)$$

Here, the energy of HeI as UV source is 21.2 eV. According to formula (1), the work functions of CdS and the interface between PANI and CdS in PANI@CdS-1 are calculated to be 3.65 and 2.86 eV, respectively, showing that the Fermi Level (E_F) has an obvious vacuum level shift (0.79 eV). In this situation, the vacuum level shift determined by the secondary electron cutoff is compensated with the interface dipole formation (Δ) as shown in Fig. 9c [38].

In vacuum, the valence band of CdS and PANI@CdS-1 is given by the formula below:

$$E_{VB}^{VACUUM} = -(E_{VBM} + \varphi). \quad (2)$$

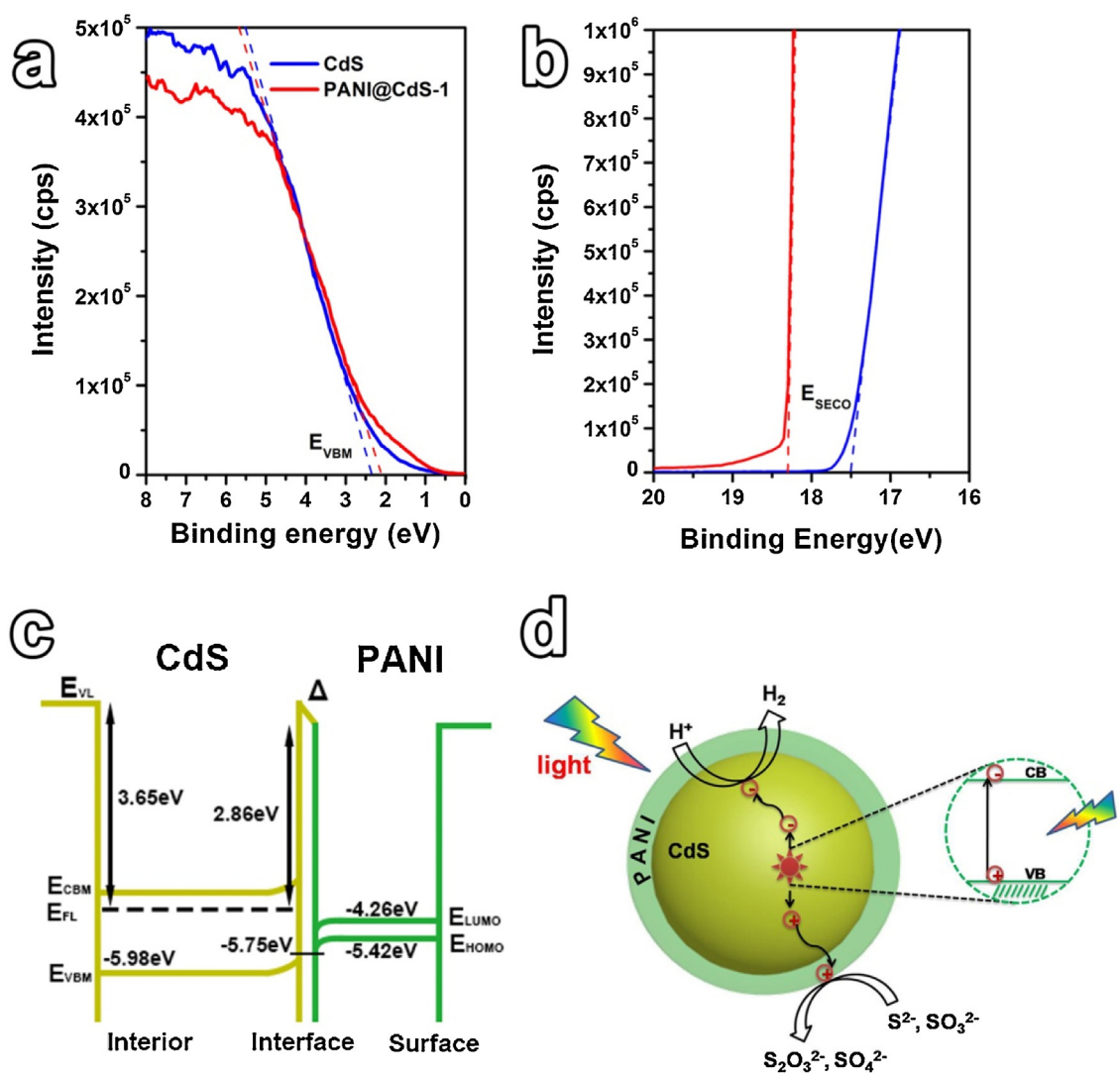

Fig. 9. UPS spectra of CdS nanospheres and PANI@CdS-1 nanospheres in (a) valence region and (b) secondary electron cutoff region. (c) Schematic energy level diagram of the component materials used in the inverted configuration, where the Vacuum Level (E_{VL}), Fermi Level (E_{FL}) and valence band (E_{VB}) positions are derived from the UPS spectra. The highest occupied molecular orbital (E_{HOMO}), lowest unoccupied molecular orbital (E_{LUMO}) and conduction band (E_{CB}) is calculated by electrochemical measuring and UV–vis absorption spectra. (d) Schematic illustrating the mechanism of CdS@PANI core-shell nanospheres for hydrogen production under visible light irradiation.

Thus the valence band $\left(E_{VB}^{VACUUM}\right)$ of CdS nanospheres and PANI@CdS-1 is at −5.98 and −5.75 eV, respectively. When the work function is identical, the bands of the CdS nanospheres surface will be flat up to the interface in thermal equilibrium. Thus the E_{VB}^{VACUUM} of CdS nanospheres surface upshifts 0.23 eV in PANI@CdS-1. Taking into account the band gap obtained from the UV–vis absorption edge, the conduction band $\left(E_{CB}^{VACUUM}\right)$ of CdS nanospheres is at −3.50 eV (a little higher than E_F). This indicates that the energy level of the CdS surface aligns with those of PANI shell with a finite shift. From the point view of thermodynamic requirements for photocatalytic reactions, the higher CB band can excite more electrons and accelerate their transport, leading to enhanced H_2 evolution.

In addition, the highest occupied molecular orbital (HOMO) and lowest unoccupied molecular orbital (LUMO) of PANI in PANI@CdS-1 locate at −5.42 and −4.26 eV respectively, according to our electrochemistry CV test illustrated in Fig. S8 [39]. In thermal equilibrium, the orbitals of PANI will be bent downward to the interface as schematically shown in Fig. 9c. As the XPS results mentioned, the CdS nanospheres exhibites behaviour of the hole-injecting semiconductor in this core-shell nanostructure. The orbitals down bent can facilitate photogenerated holes injecting into HOMO of PANI. Thus, Fig. 9d illustrates the mechanism of the PANI@CdS core-shell nanospheres, where the photogenerated electrons produce hydrogen on the surface of CdS and the photogenerated holes migrate from VB of CdS to HOMO of PANI to oxidize sacrificial reagent [40]. This significantly separates photogenerated electrons and holes, resulting in the improvement of photocatalytic hydrogen production.

4. Conclusions

Monodisperse PANI@CdS core-shell nanospheres have been designed and prepared via surface modification of the porous CdS nanospheres using proton-doped PANI to explore the mechanisms of photocatalytic hydrogen production and photocorrosion inhibition. SEM, TEM, FTIR, UV–vis, PL, XPS and UPS characterizations have been conducted on the porous CdS nanospheres and PANI@CdS core-shell nanospheres. The photocatalytic results show that the PANI@CdS core-shell nanospheres demonstrate largely enhanced photocatalytic hydrogen production and effective photocorrosion inhibition. On one hand, the newly formed C—S and/or N—S bonds between PANI and CdS prevent the surface sulfide ions reduced to sulphur, resulting in efficient photocorrosion inhibition. On the other hand, the PANI shell can effectively separate the photogenerated carriers via the photogenerated holes migrating from VB of CdS surface to HOMO of PANI, leading to improved photocatalytic hydrogen production. Furthermore, the proper PANI thickness is also very important for induced photons penetration and absorption. This work suggests that using PANI modifying CdS can improve the applications of CdS on related photocatalytic fields. In addition, our strategy may shed some light on conducting polymer modifying the photocorrosion semiconductors for enhanced photocatalytic activities and photocorrosion inhibition.

Acknowledgements

This work is realized in the frame of a program for Changjiang Scholars Innovative Research Team (IRT_15R52) of Chinese Ministry of Education. B.L. Su acknowledges the Chinese Central Government for an “Expert of the State” position in the Program of the “Thousand Talents”. Y. Li and X. Y. Yang acknowledge Hubei Provincial Department of Education for the “Chutian Scholar” program. This work is also financially supported by Hubei Provincial Natural Science Foundation (2014CFB160, 2015CFB428 and 2015CFB516), the National Science Foundation for Young Scholars of China (No. 21301133 and No. 51502225), International Science & Technology Cooperation Program of China (2015DFE52870) and Self-determined and Innovative Research Funds of the SKLWUT (2015-ZD-7).

Appendix A. Supplementary data

Supplementary data associated with this article can be found, in the online version, at http://dx.doi.org/10.1016/j.apcatb.2016.02.017.

References

[1] A. Fujishima, K. Honda, Nature 238 (1972) 37–38.
[2] X. Chen, L. Liu, P.Y. Yu, S.S. Mao, Science 331 (2011) 746–750.
[3] Q. Li, B. Guo, J.G. Yu, J.R. Ran, B.H. Zhang, H.J. Yan, J.R. Gong, J. Am. Chem. Soc. 133 (2011) 10878–10884.
[4] S.R. Lingampalli, U.K. Gautam, C.N.R. Rao, Energy Environ. Sci. 6 (2013) 3589–3594.
[5] J.R. Ran, J. Zhang, J.G. Yu, M. Jaroniec, S.Z. Qiao, Chem. Soc. Rev. 43 (2014) 7787–7812.
[6] X. Chen, C. Li, M. Gratzel, R. Kostecki, S. Mao, Chem. Soc. Rev. 41 (2012) 7909–7937.
[7] Y. Li, Z.Y. Fu, B.L. Su, Adv. Funct. Mater. 22 (2012) 4634–4667.
[8] J. Jin, J.G. Yu, G. Liu, P.K. Wong, J. Mater. Chem. A 1 (2013) 10927–10934.
[9] G. Yang, W. Yan, Q. Zhang, S. Shen, S. Ding, Nanoscale 5 (2013) 12432–12439.
[10] H.W. Park, W.Y. Choi, M.R. Hoffmann, J. Mater. Chem. 18 (2008) 2379–2385.
[11] P. Gao, J.C. Liu, S. Lee, T. Zhang, D.D. Sun, J. Mater. Chem. 22 (2012) 2292–2298.
[12] A. Ye, W. Fan, Q. Zhang, W. Deng, Y. Wang, Catal. Sci. Technol. 2 (2012) 969–978.
[13] A.B. Kaiser, V. Skakalova, Chem. Soc. Rev. 40 (2011) 3786–3801.
[14] D. Meissner, C. Benndorf, R. Memming, Appl. Surf. Sci. 27 (1987) 423–436.
[15] N.Z. Bao, L.M. Shen, T. Takata, K. Domen, Chem. Mater. 20 (2008) 110–117.
[16] X. Lu, W. Zhang, C. Wang, T.C. Wen, Y. Wei, Prog. Polym. Sci. 36 (2011) 671–712.
[17] H.D. Tran, D. Li, R.B. Kaner, Adv. Mater. 21 (2009) 1487–1499.
[18] N.M. Das, D. Roy, N. Clarke, V. Ganesanc, P.S. Gupta, RSC Adv. 4 (2014) 32490–32503.
[19] S. Zhang, Q.Y. Chen, D.W. Jing, Y.H. Wang, L.J. Guo, Int. J. Hydrogen Energy 37 (2012) 791–796.
[20] K. He, M. Li, L. Guo, Int. J. Hydrogen Energy 37 (2012) 755–759.
[21] Y.M. Lin, D.Z. Li, J.H. Hu, G.C. Xiao, J.X. Wang, W.J. Li, X.Z. Fu, J. Phys. Chem. C 116 (2012) 5764–5772.
[22] D.P. Wang, H.C. Zeng, J. Phys. Chem. C 113 (2009) 8097–8106.
[23] X.H. Li, J.X. Li, G.D. Li, D.P. Liu, J.S. Chen, Chem. Eur. J. 13 (2007) 8754–8761.
[24] W.W. Simons, The Sadtler Handbook of Infrared Spectra, Sadtler Research Laboratories, PL, 1978.
[25] Y. Li, X.Y. Yang, J. Rooke, G.V. Tendeloo, B.L. Su, J. Colloid Interface Sci. 348 (2010) 303–312.
[26] J. Liu, Z.Y. Hu, Y. Peng, H.W. Huang, Y. Li, M. Wu, X.X. Ke, G.V. Tendeloo, B.L. Su, Appl. Catal. B: Environ. 181 (2016) 138–145.
[27] M.T. Greiner, M.G. Helander, W.M. Tang, Z.B. Wang, J. Qiu, Z.H. Lu, Nat. Mater. 11 (2012) 76–81.
[28] P. Xiong, Q. Chen, M.Y. He, X.Q. Sun, X. Wang, J. Mater. Chem. 22 (2012) 17485–17493.
[29] G. Wu, C.M. Johnston, N.H. Mack, K. Artyushkova, M. Ferrandon, M. Nelson, J.S. Lezama-Pacheco, S.D. Conradson, K.L. More, D.J. Myers, P. Zelenay, J. Mater. Chem. 21 (2011) 11392–11405.
[30] B. Matteo, A. Roberto, C.A. Bignozzi, Inorg. Chem. 44 (2005) 9619–9621.
[31] H. Tong, S. Ouyang, Y. Bi, N. Umezawa, M. Oshikiri, J. Ye, Adv. Mater. 24 (2012) 229–251.
[32] W. Fan, Q. Zhang, Y. Wang, Phys. Chem. Chem. Phys. 15 (2013) 2632–2649.
[33] D.N. Ke, S.L. Liu, K. Dai, J.P. Zhou, L. Zhang, T.Y. Peng, J. Phys. Chem. C 113 (2009) 16021–16026.
[34] Y.X. Li, Y.F. Hu, S.Q. Peng, G.X. Lu, S. Li, J. Phys. Chem. C 113 (2009) 9352–9358.
[35] M. Berr, A. Vaneski, A.S. Susha, J. Rodriíguez-Fernaíndez, M. Döblinger, F. Jäckel, A.L. Rogach, J. Feldmann, Appl. Phys. Lett. 97 (2010) 093108–093111.
[36] J. Chastain, R.C. King, Handbook of X-ray Photoelectron Spectroscopy, Physical electronics, INC, 1995.
[37] E.N. Kaufmann, Characterization of Materials, Weily-Interscience, NY, 2003, pp. 2.
[38] J.J. Zhu, Z.Q. Xu, G.Q. Fan, S.T. Lee, Y.Q. Li, J.X. Tang, Org. Electron. 12 (2011) 2151–2158.
[39] C.M. Cardona, W. Li, A.E. Kaifer, D. Stockdale, G.C. Bazan, Adv. Mater. 23 (2011) 2367–2371.
[40] Z. Zhang, T.Y. John, Chem. Rev. 112 (2012) 5520–5551.